Russian Geology and Geophysics © 2020, V.S. Sobolev IGM, Siberian Branch of the RAS
Vol. 61, No. 5–6, pp. 571–591, 2020 *DOI:10.15372/RGG2019177* *Geologiya i Geofizika*

Melting and Parageneses of Global Subducting Water-Enriched Sediment in Closed and Open Systems: Experiment and Thermodynamic Modeling

A.L. Perchuk[a,b,] ✉, A.A. Serdyuk[b], N.G. Zinovieva[a], M.Yu. Shur[a]

[a] *Lomonosov Moscow State University, Leninskie Gory 1, Moscow, 119234, Russia*

[b] *D.S. Korzhinskii Institute of Experimental Mineralogy, Russian Academy of Sciences, Chernogolovka, Moscow Region, 142432, Russia*

Received 30 April 2019; accepted 28 August 2019

Abstract—The phase relations and melting of subducting sediment were studied in two series of high-pressure experiments at 750–900 ºC and 2.9 GPa and by thermodynamic modeling. In the runs we used a chemical mixture corresponding in composition to global subducting sediment (GLOSS) but enriched in water (H_2O = 15.52 wt.% as compared with 7.29 wt.% in GLOSS). The first series of runs was carried out in open capsules, and the second series was performed by the same procedure and at the same *P–T–t* parameters but in closed (welded) capsules. The products of the runs of both series showed agreement on the *P–T* conditions of melting and the presence of garnet, carbonate, kyanite, SiO_2 phase, and phengite in the parageneses. However, the products of all runs in open capsules contain omphacite, including magmatic one, whereas the products of the runs in welded capsules lack it, except for those obtained in the subsolidus run (at 750 ºC). The results of thermodynamic modeling for the composition of the experimental mixture (H_2O–GLOSS) in the closed system are in agreement with the experimental data on the hydrous solidus and the stability of most minerals, showing a decrease in the content of omphacite as melt appears. This specific effect caused by the increased pressure of aqueous fluid in the closed system is observed in the welded capsules. Thermodynamic modeling for the H_2O–GLOSS composition also shows that a complete decomposition of slab carbonates under "hot" subduction conditions is possible, but this result is not confirmed by our experimental data. Since the melting and mineral growth processes in subduction zones are controlled by migrating fluids and melts, it seems correct to rely on the results of runs in open capsules.

Keywords: subducting sediment, experiment, subduction, melting, thermodynamic modeling open and closed systems

INTRODUCTION

Magmatism, metamorphism, metasomatism, and intraplate earthquakes in subduction zones are substantially controlled by aqueous fluid released by decomposition of the hydrous minerals of subducting oceanic plates (Tatsumi and Eggins, 1995; Schmidt and Poli, 1998). Considerable quantities of water, silicon, aluminum, LILE, LREE, and carbonates penetrating subduction zones are contained in the upper oceanic crust (Scambelluri and Philippot, 2001; Hermann et al., 2006; Bebout, 2007; Spandler and Pirard, 2013; Zheng, 2019). Here the chemo- and biogenic deep-water sediments of the ocean floor coexist with large masses of terrigenous sediments transported from island arcs or continental margins to trenches and accretionary prisms. The sediment thicknesses and rock compositions in them are so diverse and vary so greatly from one subduction zone to another (Plank and Langmuir, 1998) that no natural sediment can be chosen as representative for subduction zones. Therefore, statistical processing of the compositions, structures, and thicknesses of sediment strata in numerous subduction zones was carried out to obtain the composition of the average subducting sediment—GLOSS (Global Subducting Sediment (Plank and Langmuir, 1998)). This composition was used extensively in studies, such as estimation of dehydration and decarbonation in subducting slabs by petrological–thermomechanical modeling (Gonzalez et al., 2016) and thermodynamic modeling of phase equilibria in subducting sediments in closed and open systems (Kerrick and Connolly, 2001a,b; Gorman et al., 2006).

Besides that, GLOSS had an application in experimental studies (Table 1). For example, its melting in the presence of graphite and diamond at 7.5–12 GPa and 800–1600 °C was studied (Brey et al., 2015), and its interaction with mantle substrates at $P > 2.9$ GPa and a wide range of temperatures was modeled (Bulatov et al., 2014; Woodland et al., 2018; Perchuk et al., 2019). Also, more aluminous compositions of subducting sediment (Table 1) were used in experimental studies of phase relations and melting (Hermann and Spandler, 2008; Grassi and Schmidt, 2011).

Changes in H_2O and CO_2 contents in subducting plates (including sediments) are the most important component of the budget of these volatiles in subduction zones; they were estimated based on the thermal structure of subduction zones and experimental and thermodynamic data on the

✉ Corresponding author.
E-mail address: alp@geol.msu.ru (A.L. Perchuk)

Table 1. Chemical compositions (wt.%) of GLOSS and the mixtures used in experimental studies

Component	Composition									
	GLOSS	SS*	H_2O–GLOSS **	EPSM	EPSM	DG2	AM	Na–GLOSS	K–GLOSS	K–GLOSS
	(Plank and Langmuir, 1998)	(Perchuk et al., 2019; this study)		(Hermann and Spandler, 2008)		(Grassi and Schmidt, 2011)		(Brey et al., 2015; Bulatov et al., 2014)		(Woodland et al., 2018)
SiO_2	58.57	52.74	53.10	68.83	64.15	54.63	47.6	56.8	56.9	65.8
TiO_2	0.62	0.57	0.57	0.67	0.63	0.63	n.d.	0.6	0.6	0.74
Al_2O_3	11.91	10.76	10.83	14.7	13.7	20.23	22.8	11.6	11.6	11.2
Cr_2O_3	<0.01	<0.01	<0.01	n.d.	n.d.	n.d.	n.d.	n.d.	n.d.	0
FeO	5.21	n.d.	5.03	4.67	4.35	4.86	9.2	n.d.	n.d.	n.d.
Fe_2O_3	n.d.	5.55	n.d.	n.d.	n.d.	n.d.	n.d.	n.d.	n.d.	n.d.
FeO_{tot}	n.d.	n.d.	n.d.	n.d.	n.d.	n.d.	n.d.	5.07	5.07	6.43
MnO	0.32	0.01	0.01	0.11	0.1	n.d.	n.d.	n.d.	n.d.	0
MgO	2.48	2.33	2.35	2.51	2.34	2.92	2	2.41	2.41	3.4
CaO	5.95	5.32	5.36	2.45	2.28	5.88	6.8	5.8	5.8	6.5
Na_2O	2.43	2.26	2.28	2.62	2.44	3.2	2.4	2.4	1	1.32
K_2O	2.04	1.71	1.72	2.94	2.74	2.21	3.6	2	3.4	4
P_2O_5	0.19	0.19	0.19	0.32	0.3	n.d.	n.d.	0.18	0.18	0.28
H_2O	7.29	n.d.	15.52	n.d.	6.8	n.d.	1.1	6.9	6.9	6.9
CO_2	3.01	n.d.	3.01	n.d.	n.d.	4.5	4.8	6	5.9	5.9
Total	100.02	81.44	99.97	99.8	99.81	99.07	100.3	100	100	100

Note. n.d., Not determined.
*X-ray fluorescence analysis of the initial mixture, D.S. Korzhinskii Institute of Experimental Mineralogy (analyst A.I. Yakushev). LOI = 18.53 wt.%.
**Composition of the initial mixture which was used in thermodynamic calculations based on XRF analysis (SS composition), recalculated for FeO and with regard to CO_2 and H_2O contents in the specimen.

phase equilibria and stability of minerals in different lithologic types of slab rocks (Schmidt and Poli, 1998; van Keken et al., 2011).

We compared experimental and thermodynamic data obtained for the same GLOSS composition under the *P–T* conditions of nearly isobaric heating of the slab surface in a hot subduction zone (Syracuse et al., 2010). The modeling was carried out with regard to partial melting, which has a substantial influence on parageneses and the content of volatiles in rock. Another feature of our study was the use of different experimental methods which permit comparing the effects of closed and open systems, parageneses, and the compositions of parental melts.

EXPERIMENTAL

Subducting sediment. A chemical mixture of composition H_2O–GLOSS (Table 1) obtained from at least 99% pure powdered oxides, hydroxides, and salts (Aldrich products, www.sigmaaldrich.com) was used in the runs. The reagents were chosen so that their combination in a certain proportion would yield the required composition corresponding to GLOSS (Plank and Langmuir, 1998). Global subducting sediment was obtained as follows. Phosphorus was introduced into the system as KH_2PO_4; magnesium, as compound $4MgCO_3 \cdot Mg(OH)_2 \cdot 5H_2O$. Remaining CO_2 was added as K_2CO_3. Lacking potassium was added as KOH. The necessary amount of water was introduced first as NaOH (its quantity was determined by the required Na content) and then as $Al(OH)_3$. The rest of Al was added as Al_2O_3. The other elements were introduced in the required quantity as oxides SiO_2, TiO_2, FeO, MnO, and CaO. Thus, the composition of the mixture used in the runs corresponded to that of GLOSS (Plank and Langmuir, 1998) in terms of the relative contents of all the components except H_2O. The high H_2O content of the initial mixture (H_2O–GLOSS composition, calculated based on X-ray fluorescence analysis (Table 1)), resulting from the sorption of atmospheric water (NaOH and K_2CO_3 as the main sorbents), was favorable for mineral reactions and melting. Also, this is similar to the natural conditions in a slab because of the existence of several sources of aqueous fluid under the subducted sediment strata (Spandler and Pirard, 2013).

Experimental method. Powdered subducting sediment (H_2O–GLOSS (Table 1)) was placed in 3 mm long $Ag_{30}Pd_{70}$ capsules with an external diameter of 2 mm. The runs were performed by two techniques at the same temperatures and pressures: involving welded capsules and involving capsules without upper lids. The capsules with no upper lids, which had been used in (Perchuk et al., 2018a), reproduce near-natural single fluid (melt) flux through the studied substance. Otherwise, as the fluid (melt) remains in the capsule for a long time, it can move upward and downward or remain still. Each capsule was located in the gradientless zone of a high-pressure cell. The structure of the salt cell and the position of the capsule are shown in Fig. 1. The capsule was placed in

Table 2. Conditions and products of runs with subducting sediment (H_2O–GLOSS) at P = 2.9 GPa

Run no.	T, °C	Time, h	Phase association*		
			Zone I	Zone II	Zone III
Open capsules					
ss19	750	216	Dol, Ky, SiO_2, Phn	Dol, SiO_2	Grt, Omp
ss5	800	132	Mgs, Omp, SiO_2, Phn	Grt, Mgs, Omp, L, Ky, SiO_2 (single zone)	
ss17	850	144	Grt, Dol, Omp, L, Ky, SiO_2, Phn (single zone)		
ss18	900	144	Grt, Dol, Omp, L (single zone)		
Welded capsules					
ss6	750	216	Grt, Dol, Omp, Ky, SiO_2, Phn (single zone)		
ss7	800	120	Grt, L, Dol, Ky, SiO_2, Phn	Grt, L (single zone)	
ss2	850	144	Grt, Dol, L, Ky, SiO_2, Phn	Grt, L	L
ss3	900	144	Grt, Dol, L, Ky, SiO_2	Grt, L	L

Note. *Abbreviations (hereinafter): Ank, ankerite; Arag, aragonite; Bi, biotite; Carb, carbonates; Coe, coesite; Cpx, clinopyroxene; Dol, dolomite; Grt, garnet; Kfs, K-feldspar; Ky, kyanite; L, liquid (glass); Law, lawsonite; Mgs, magnesite; Mica, mica (muscovite); Omp, omphacite; Opx, orthopyroxene; Phn, phengite; Q, quartz; SiO_2, SiO_2 phase.

the zone of the least temperature gradient. The capsule and thermocouple inside the cell were placed in pressed MgO.

The runs were carried out using a cylinder–piston setup at Korzhinskii Institute of Experimental Mineralogy at 750–900 °C and 2.9 GPa (Table 2), which corresponds to the geotherms at the crust–mantle boundary obtained by thermomechanical modeling for hot subduction zones (model D80) from (Syracuse et al., 2010). The duration of the runs was chosen in correspondence with the previous runs, in which dry amphibolite and blueschist powders were the source of fluids (melts) and the Grt–Cpx geothermometry of the newly formed phases reproduced the temperatures from (Perchuk et al., 2018a,b). The information on the pressure calibration of the setup is given in (Perchuk et al., 2013). Oxygen fugacity in the runs was not controlled. According to (Patiño Douce and Harris, 1998), cells with a graphite heater limit f_{O_2} in the sample between the FMQ and FMQ-2 buffers, which corresponds to the conditions estimated for peridotites of the suprasubduction mantle (Foley, 2011). The duration of the runs varied from 120 to 216 h; low-temperature runs lasted for a longer time than high-temperature ones because of the differences in the kinetics of mineral growth at different temperatures (Table 2). Temperature was measured using the WRe5/20 thermocouple on top of the capsule.

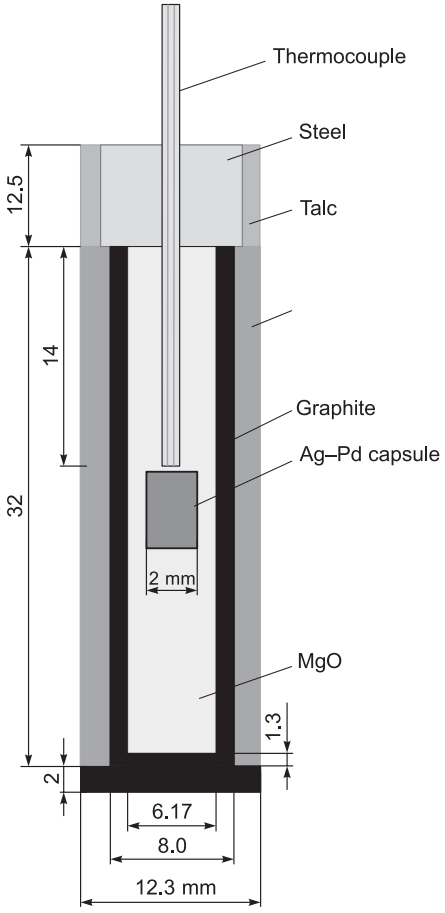

Fig. 1. Scheme of pressure cell.

After the runs the capsules were put in polystyrene pellets and polished on diamond wheels and pastes.

ANALYTICAL METHODS

Electron microscopic studies and electron microprobe analysis of minerals and glasses were made in the Laboratory of Local Methods of Substance Study (Department of Petrology and Volcanology, Faculty of Geology, Lomonosov Moscow State University).

Chemical analyses of phases were performed using a Superprobe JXA-8230 with a wolfram thermionic cathode. The structural relations between the experimental phases were studied in the BSE mode at an accelerating voltage of 20 kV. Quantitative microanalysis of minerals with the use of five wave dispersion spectrometers was carried out in the

mode of the focused electron probe at an accelerating voltage of 20 kV and a current of 20 nA. To analyze glasses, micas, and carbonates, the electron probe was defocused to 6–10 μm. Natural silicates were used as standards for measurement of major elements. The pulse accumulation time for major elements was 30 s at the peak and 15 s on the background. Under these conditions the standard deviation for major components was no more than 0.9 rel.%.

A part of the analyses was performed on a Jeol JSM-6480LV SEM with an Oxford X-MaxN EDS using the same standards. Back-scattered electron images were obtained at 20 kV. Local quantitative energy-dispersive analysis of phases was made at 20 kV and 10 nA. Glasses were analyzed with a rasterized (defocused) beam to avoid alkali loss.

The contents of major components in powders of the original rocks were determined by XRF analysis on a Philips PW 2400 spectrometer at the Institute of Geology of Ore Deposits, Petrography, Mineralogy, and Geochemistry (Moscow).

RESULTS

Taking into account the differences between the run products (Fig. 2; Table 2), we consider phase relations for each set separately.

Products of runs in open capsules. The open capsules were slightly deformed after the runs because of vertical compression, but they retained the cylindric shape (Fig. 2*a–d*).

The run temperature had a substantial influence on the spatial distribution of phases (melt and minerals) and parageneses (Fig. 2; Table 2). For example, as temperature decreases, the even distribution of minerals (garnet, omphacite, and carbonate) in melt at 900 °C is followed by vertical zoning till the appearance of three zones with different parageneses at 750 °C (Fig. 3). Note that the products of all the runs contain garnet, omphacite, and carbonate. Melt is missing only from the lowest temperature run; on the contrary, phengite and SiO_2 phase are missing from the highest temperature run (900 °C). In this set of runs, SiO_2 phase was not determined, but quartz had been found in the products of the runs under the same *P–T* conditions using a HORIBA Scientific XPloRA Raman spectrometer with a confocal microscope (Perchuk et al., 2018a), which is consistent with the experimental data in (Bose and Ganguly, 1995).

Minerals in the runs at $T \geq 850$ °C grow from melt and usually exhibit idiomorphic shape (Fig. 4). Glasses are porous, but narrow zones around the minerals are poreless (Fig. 4). In the run at 800 °C, melt is located only at the

Table 3. Representative electron microprobe analyses of clinopyroxene from the products of runs at $P = 2.9$ GPa

Component	Run no., *T*, °C						
	ss19, 750	ss5, 800	ss17, 850		ss18, 900		ss6, 750
	Open capsule						Welded capsule
SiO_2, wt.%	55.36	53.97	54.48	54.01	54.10	53.64	53.65
TiO_2	0.21	0.57	0.40	0.18	0.15	0.39	0.29
Al_2O_3	13.79	15.35	11.75	8.08	3.48	8.08	14.79
Cr_2O_3	b.d.l.	b.d.l.	b.d.l.	b.d.l.	b.d.l.	b.d.l.	b.d.l.
FeO	5.64	7.43	2.89	3.60	4.50	3.75	8.82
MnO	b.d.l.	b.d.l.	b.d.l.	b.d.l.	b.d.l.	b.d.l.	b.d.l.
MgO	6.11	4.80	9.97	12.05	15.51	12.34	3.64
CaO	10.62	9.75	15.25	17.78	20.53	18.01	7.80
Na_2O	7.36	7.34	5.20	4.00	1.72	3.26	8.48
K_2O	b.d.l.	b.d.l.	b.d.l.	b.d.l.	b.d.l.	b.d.l.	b.d.l.
Total	99.09	99.21	99.94	99.70	99.99	99.47	97.47
Crystal-chemical formula							
O, p.f.u.	6	6	6	6	6	6	6
Si	1.98	1.94	1.93	1.95	1.96	1.93	1.97
Ti	0.01	0.02	0.01	0.00	0.00	0.01	0.01
Al	0.58	0.65	0.49	0.34	0.15	0.34	0.64
Cr	b.d.l.	b.d.l.	b.d.l.	b.d.l.	b.d.l.	b.d.l.	b.d.l.
Fe^{3+}	0.00	0.00	0.00	0.00	0.06	0.02	0.03
Fe^{2+}	0.17	0.22	0.09	0.11	0.08	0.10	0.24
Mn	b.d.l.	b.d.l.	b.d.l.	b.d.l.	b.d.l.	b.d.l.	b.d.l.
Mg	0.33	0.26	0.53	0.65	0.84	0.66	0.20
Ca	0.41	0.38	0.58	0.69	0.80	0.70	0.31
Na	0.51	0.51	0.36	0.28	0.12	0.23	0.60
K	b.d.l.	b.d.l.	b.d.l.	b.d.l.	b.d.l.	b.d.l.	b.d.l.
X_{Mg}	0.66	0.54	0.86	0.86	0.92	0.87	0.45
X_{Jd}	0.51	0.51	0.36	0.24	0.06	0.21	0.57

Note. Hereinafter: b.d.l., below detection limit. $X_{Mg} = Mg/(Mg + Fe^{2+})$ with regard to Fe^{3+}. X_{Jd}, Mole fraction of the jadeite end-member.

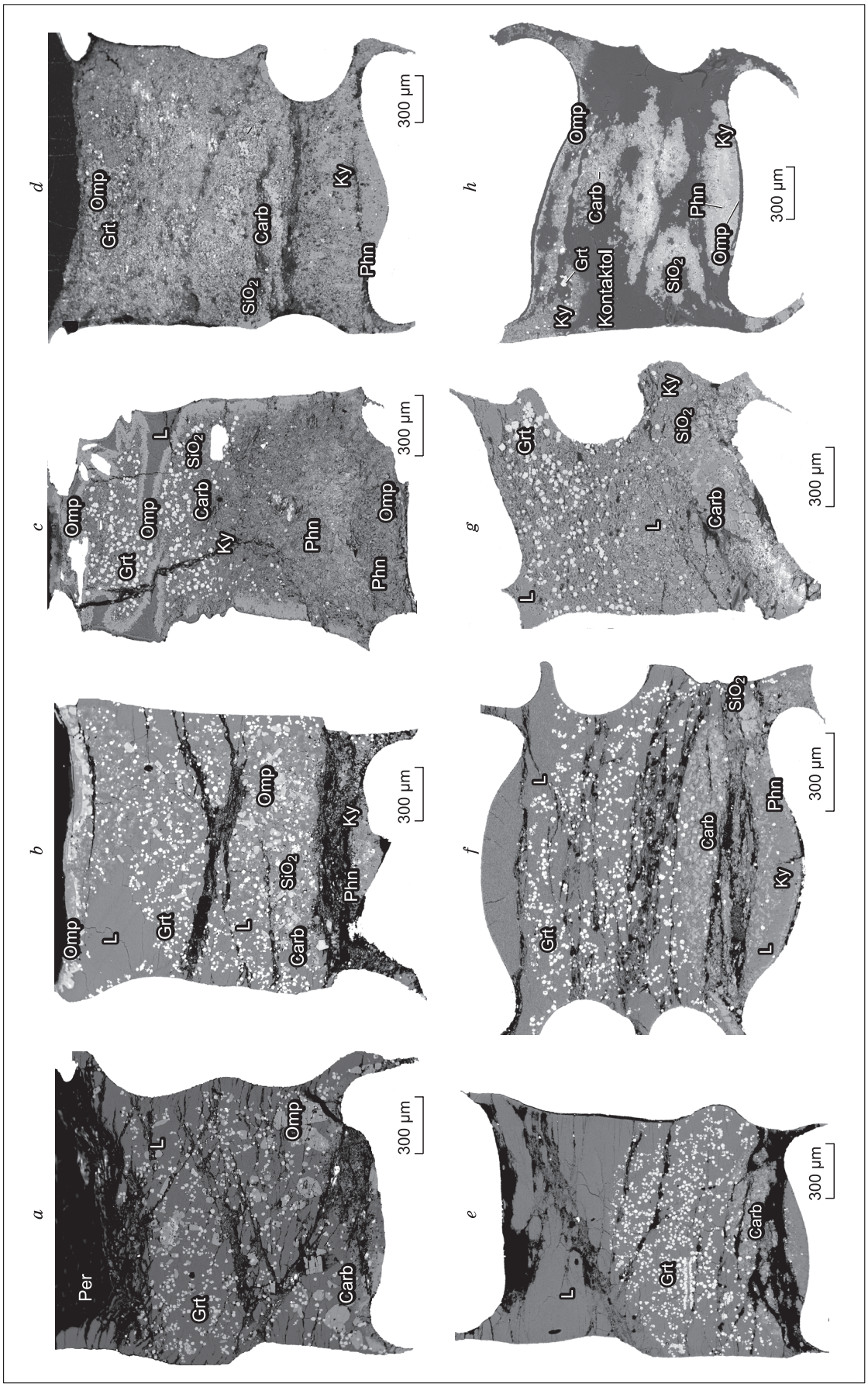

Fig. 2. Capsules with subducting sediment (H_2O–Global Subducting Sediment (GLOSS) (Table 1)) after runs at 2.9 GPa and different temperatures.
Open capsules: *a*, 900 °C (run ss18); *b*, 850 °C (ss17); *c*, 800 °C (ss5); *d*, 750 °C (ss19). Welded capsules: *e*, 900 °C (run ss3); *f*, 850 °C (ss2); *g*, 800 °C (ss7); *h*, 750 °C (ss6). Back-scattered electron images. The number of run and temperature are shown for each capsule. In open capsules subducting sediment is in contact with periclase (Per). See details in the text.

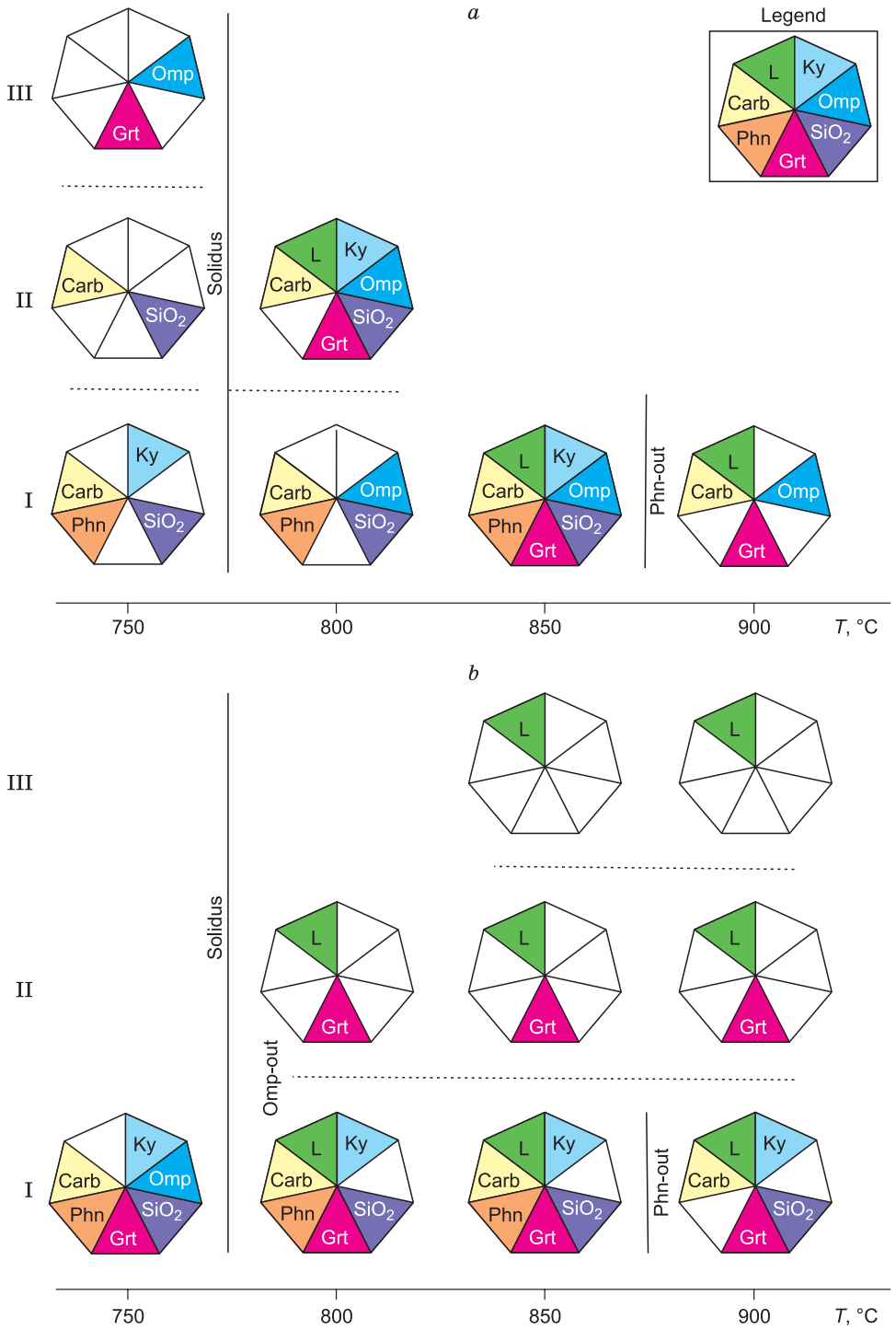

Fig. 3. Phase associations in different zones of the products of runs at 750–900 °C and 2.9 GPa: *a*, Open capsules, no zoning (single zone) in the runs at 850 and 900 °C and a single upper zone (II–III) in the run at 800 °C; *b*, welded capsules, no zoning (single zone) in the run at 750 °C and a single upper zone (II–III) in the run at 800 °C. Rock-forming minerals are shown in the filled sectors of polyhedra. Zonal boundaries are marked by dotted lines. See details in the text.

capsule top. Here it forms narrow "embayments" rimmed with omphacite aggregate, which begin near the capsule walls, or is in assemblage with garnet, omphacite, kyanite, phengite, carbonate, and SiO_2 phase (Fig. 4).

Products of runs in welded capsules. The welded capsules were somewhat more deformed than the open ones in same-temperature runs (Fig. 2*e–h*). The capsule in the lowest temperature run exhibits the best retained shape.

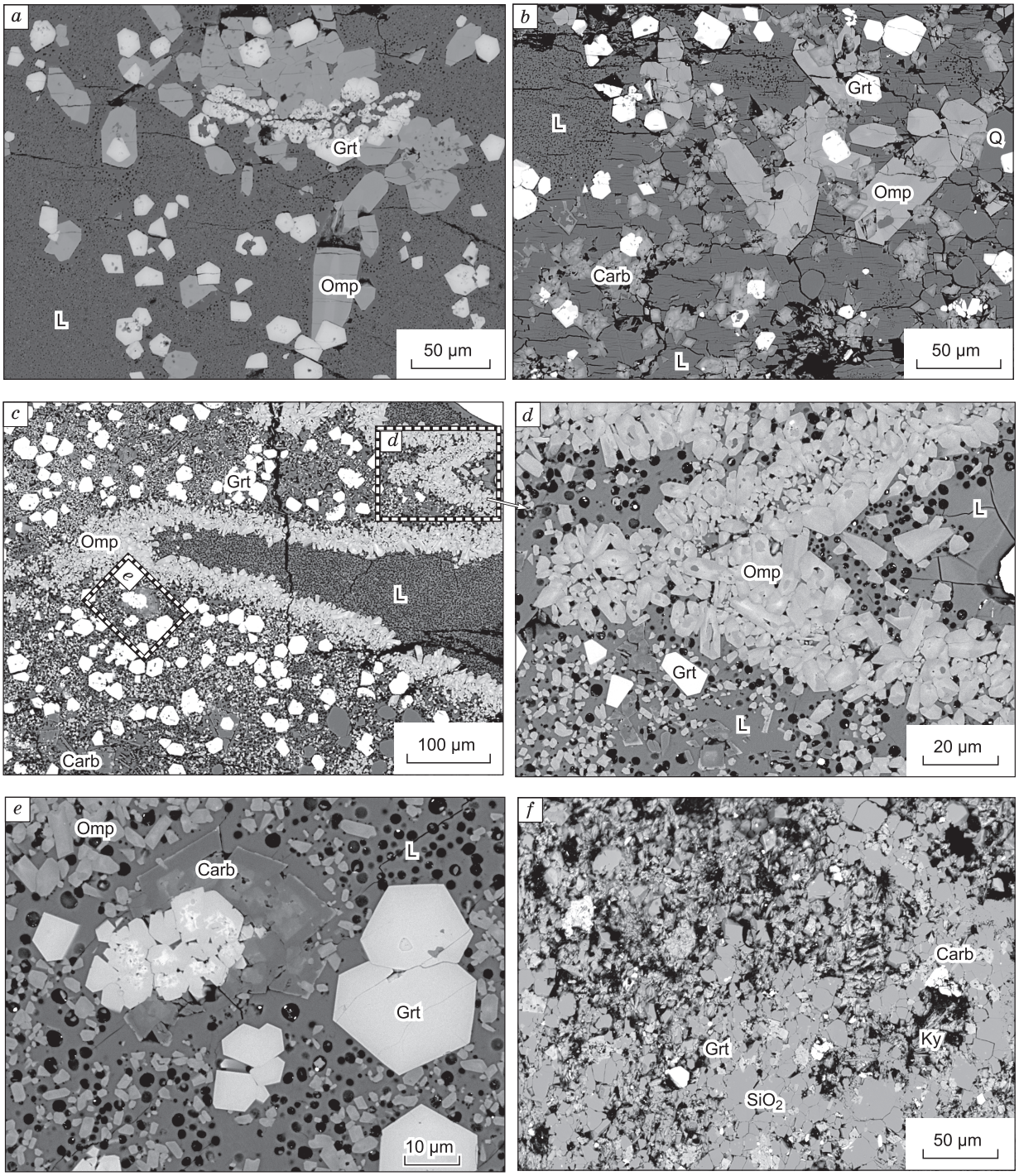

Fig. 4. Phase relations in the run products from open capsules at 2.9 GPa and different temperatures. *a*, Idiomorphic garnet and omphacite crystals in glass at 900 °C (run ss18); *b*, idiomorphic garnet, omphacite, and zoned carbonate crystals in glass at 850 °C (ss17); *c*, apophyses of wall-side melt surrounded by omphacite aggregates at 800 °C (ss5). *d*, aggregate of idiomorphic omphacite grains in porous glass at 800 °C (ss5); *e*, zoned garnet, omphacite, and carbonate crystals in porous glass at 800 °C (ss5); *f*, fragment of zone I from the run at 750 °C (ss19). Back-scattered electron images hereinafter; the mineral composition of zones is shown in Table 2 and Fig. 3.

The products of this set of runs show distinct vertical zoning (Figs. 2*e–g*, 5), which is mainly due to the segregation of melt on top of the capsules. As temperature decreases, the content of melt (glass) decreases to zero at 750 °C (Fig. 4), which is ~50 °C higher than the hydrous solidus of subducted pelites (Hermann and Spandler, 2008) and >50 °C lower than that of carbonated pelites (Grassi and Schmidt, 2011). Melt from the middle zone contains evenly distrib-

Table 4. Representative electron microprobe analyses of garnets from the products of runs at P = 2.9 GPa

Component	Run no., T, °C												
	ss19, 750	ss5, 800		ss17, 850		ss18, 900	ss6, 750	ss7, 800		ss2, 850		ss3, 900	
	Open capsule						Welded capsule						
	III	II (c*)	II (r*)	I** (c)	I** (r)	I**	I**	II	III	II	III	II	III
SiO_2, wt.%	37.83	37.31	37.95	38.36	38.61	38.10	36.49	37.81	37.25	37.31	38.78	37.74	38.56
TiO_2	0.40	0.86	0.62	1.10	0.70	0.84	0.45	0.85	0.90	0.92	0.43	1.12	0.50
Al_2O_3	20.98	20.90	21.04	21.24	21.76	20.53	20.22	21.41	20.95	20.71	21.83	20.76	22.08
Cr_2O_3	b.d.l.	b.d.l.	b.d.l.	b.d.l.	b.d.l.	b.d.l.	b.d.l.	b.d.l.	b.d.l.	b.d.l.	b.d.l.	b.d.l.	b.d.l.
FeO	25.39	25.99	24.62	22.17	19.53	24.45	27.17	27.08	27.09	25.71	25.43	25.07	22.42
MnO	0.06	0.06	0.05	0.04	b.d.l.	0.04	0.09	0.05	0.04	0.07	0.12	b.d.l.	b.d.l.
MgO	3.88	3.36	5.23	5.90	8.25	6.01	2.95	2.90	2.58	4.12	5.87	5.28	6.93
CaO	9.80	10.01	9.24	10.26	9.93	9.14	8.77	9.59	9.97	9.22	8.06	8.98	8.95
Na_2O	0.07	0.15	0.09	0.13	0.11	0.06	0.11	0.14	0.13	0.13	0.12	0.17	0.15
K_2O	b.d.l.	b.d.l.	b.d.l.	b.d.l.	b.d.l.	b.d.l.	b.d.l.	b.d.l.	b.d.l.	b.d.l.	b.d.l.	b.d.l.	b.d.l.
Total	98.42	98.64	98.84	99.20	98.93	99.18	96.25	99.82	98.90	98.18	100.64	99.15	99.64
Crystal-chemical formula													
O, p.f.u.	12	12	12	12	12	12	12	12	12	12	12	12	12
Si	3.00	2.97	2.98	2.98	2.96	2.98	2.99	2.98	2.98	2.98	2.99	2.96	2.97
Ti	0.02	1.96	1.95	0.06	0.04	0.05	0.03	0.05	0.05	0.06	0.02	0.07	0.03
Al	1.96	0.00	0.00	1.94	1.97	1.89	1.96	1.99	1.97	1.95	1.98	1.92	2.00
Cr	b.d.l.	b.d.l.	b.d.l.	b.d.l.	b.d.l.	b.d.l.	b.d.l.	b.d.l.	b.d.l.	b.d.l.	b.d.l.	b.d.l.	b.d.l.
Fe^{3+}	0.01	0.01	0.03	0.01	0.03	0.08	0.02	0.00	0.00	0.02	0.00	0.05	0.00
Fe^{2+}	1.67	1.72	1.59	1.43	1.23	1.51	1.84	1.79	1.81	1.69	1.64	1.60	1.44
Mn	0.00	0.00	0.00	0.00	b.d.l.	0.00	0.01	0.00	0.00	0.00	0.01	b.d.l.	b.d.l.
Mg	0.46	0.40	0.61	0.68	0.94	0.70	0.36	0.34	0.31	0.49	0.67	0.62	0.80
Ca	0.83	0.85	0.78	0.85	0.82	0.77	0.77	0.81	0.85	0.79	0.67	0.76	0.74
Na	0.01	0.02	0.01	0.02	0.02	0.01	0.02	0.02	0.02	0.02	0.02	0.03	0.02
K	b.d.l.	b.d.l.	b.d.l.	b.d.l.	b.d.l.	b.d.l.	b.d.l.	b.d.l.	b.d.l.	b.d.l.	b.d.l.	b.d.l.	b.d.l.
X_{Mg}	0.22	0.19	0.28	0.32	0.43	0.32	0.16	0.16	0.15	0.22	0.29	0.28	0.36
X_{Ca}	0.28	0.29	0.26	0.29	0.27	0.26	0.26	0.28	0.29	0.26	0.22	0.25	0.25
Alm	0.41	0.58	0.53	0.51	0.48	0.56	0.62	0.61	0.61	0.57	0.55	0.54	0.48
Prp	0.32	0.13	0.21	0.23	0.23	0.15	0.12	0.12	0.10	0.16	0.23	0.21	0.27
Grs	0.27	0.29	0.26	0.26	0.29	0.28	0.26	0.28	0.29	0.26	0.22	0.25	0.25

Note. X_{Mg} = Mg/(Mg + Fe^{2+}); X_{Ca}= Ca/(Ca + Mg + Fe^{2+}) with regard to Fe^{3+}.
*c, core; r, rim.
**Unzoned capsule.

uted magmatic garnet. Its crystals are generally idiomorphic, often poikilitic. At the upper boundary of this zone, atoll or skeletal crystals are detected (Fig. 6*a*, *c*). Also, small areas of melt are preserved in the lower zone, coexisting with garnet, carbonate, kyanite, SiO_2 phase, and phengite (Fig. 6*b*, *e*, *f*). Phengite is observed in all the runs except that with the highest temperature. In the lowest temperature run, the capsules show no zoning; also, melt is absent, but omphacite appears, coexisting with garnet, carbonate, kyanite, SiO_2 phase, and phengite (Fig. 4).

Thus, the products of both sets of runs are characterized by coinciding positions of the hydrous solidus and phengite stability field as well as the presence of carbonates and garnet. A part of the carbonates might be quenched crystals. The most important difference is that the products of most of the runs in welded capsules do not contain omphacite, which is widespread in all the runs in open capsules.

Phase compositions. Representative analyses of minerals are given in Tables 3–7. Electron microprobe analyses were recalculated using the oxygen method with regard to ferric iron (Fe^{3+}) for garnet and clinopyroxene.

Clinopyroxene is detected in the products of all the runs in open capsules, but only at 750 °C in welded capsules. It mainly corresponds to omphacite (X_{Mg} = 0.47–0.98, and X_{Jd} = 0.10–0.53), but zoned clinopyroxene crystals (block zoning) in the run at 900 °C contain areas with the composi-

Table 5. Representative electron microprobe analyses of glasses from the products of runs at P = 2.9 GPa

Component	Run no., T, °C					
	ss5, 800	ss17, 850	ss18, 900	ss7, 800	ss2, 850	ss3, 900
	Open capsule			Welded capsule		
Analyses are normalized to 100%						
SiO_2, wt.%	76.71	76.54	74.65	75.01	75.16	74.54
TiO_2	0.11	0.16	0.30	0.20	0.21	0.24
Al_2O_3	14.16	14.25	13.64	14.84	13.77	14.14
Cr_2O_3	b.d.l.	b.d.l.	b.d.l.	b.d.l.	b.d.l.	b.d.l.
FeO	0.71	0.62	0.98	0.64	0.97	0.96
MnO	b.d.l.	b.d.l.	b.d.l.	b.d.l.	b.d.l.	b.d.l.
MgO	0.45	0.53	0.89	0.34	0.32	0.5
CaO	1.77	1.86	2.64	1.00	1.28	2.14
Na_2O	2.89	2.13	3.12	4.49	4.08	3.79
K_2O	3.19	3.89	3.77	3.50	4.22	3.65
Total without H_2O	86.58	89.03	87.721	83.9	84.46	83.45
K_2O+Na_2O	6.08	6.02	6.88	7.98	8.3	7.44
K_2O/Na_2O	1.10	1.82	1.21	0.78	1.03	0.97

Table 6. Representative electron microprobe analyses of carbonates from the products of runs at P = 2.9 GPa

Component	Run no., T, °C							
	ss19, 750	ss5, 800	ss17, 850	ss18, 900	ss6, 750	ss7, 800	ss2, 850	ss3, 900
	Open capsule				Welded capsule			
FeO, wt.%	11.48	16.36	8.03	7.26	13.95	12.82	9.88	6.73
MnO	b.d.l.	b.d.l.	b.d.l.	b.d.l.	b.d.l.	b.d.l.	0.20	b.d.l.
MgO	12.22	30.07	16.79	15.92	10.33	11.06	12.61	7.91
CaO	29.79	4.30	30.32	30.13	27.07	28.74	28.88	22.39
Total	54.75	50.97	55.44	53.53	52.32	53.07	54.15	37.34
	Crystal-chemical formula							
O, p.f.u.	1	1	1	1	1	1	1	1
Fe^{2+}	0.15	0.22	0.10	0.10	0.20	0.18	0.13	0.13
Mn	b.d.l.	b.d.l.	b.d.l.	b.d.l.	b.d.l.	b.d.l.	0.00	b.d.l.
Mg	0.29	0.71	0.39	0.38	0.27	0.28	0.30	0.28
Ca	0.51	0.07	0.50	0.52	0.50	0.52	0.49	0.57
X_{Mg}	0.65	0.77	0.79	0.80	0.57	0.61	0.69	0.68
X_{Ca}	0.53	0.07	0.51	0.52	0.52	0.53	0.53	0.58

Note. X_{Mg} = Mg/(Mg + Fe^{2+}); X_{Ca}= Ca/(Ca + Mg + Fe^{2+} + Mn).

tion parameters (X_{Mg} = 0.92–0.96, and X_{Jd} = 0.03–0.09) corresponding to those of augite (Fig. 7; Table 3). The composition parameters of omphacite in open capsules are marked by an increase in X_{Mg} and a decrease in jadeite content with increasing temperature. Omphacites from a welded capsule at 750 °C, like those from a same-temperature run in an open capsule, are characterized by low X_{Mg} (0.40–0.47) and high X_{Jd} (0.57–0.61) (Fig. 7; Table 3).

Garnet is present in all the runs regardless of the capsule type. Its modal content increases as the run temperature increases. Compositionally, it belongs to the almandine–pyrope–grossular series of solid solution in which X_{Mg} = 0.15–0.51, and X_{Ca} = 0.19–0.31 (Fig. 8; Table 4), with a low TiO_2 (schorlomite end-member) content. Garnet is characterized by higher X_{Mg} as the run temperature increases. The garnet grains sometimes show concentric growth zoning with higher X_{Mg} and lower X_{Ca} from core to rim (Fig. 8; Table 4).

Melts (glasses) are observed in all the runs at $T \geq 800$ °C, and they are rhyolitic (Fig. 9; Table 5). Melts within one capsule vary in SiO_2, Na_2O, and K_2O contents within 1–2 wt.% (Fig. 9), but no zoning or pattern is found in the compositional variation. Low oxide totals suggest the pres-

Table 7. Representative electron microprobe analyses of phengite from the products of runs at P = 2.9 GPa

Component	Run no., T, °C					
	ss19, 750	ss5, 800	ss17, 850	ss6, 750	ss7, 800	ss2, 850
	Open capsule			Welded capsule		
SiO_2, wt.%	51.79	51.12	48.30	50.53	51.99	51.64
TiO_2	0.44	0.52	1.10	0.47	0.74	0.67
Al_2O_3	28.40	28.51	31.73	29.53	28.32	29.45
Cr_2O_3	b.d.l.	b.d.l.	b.d.l.	b.d.l.	b.d.l.	b.d.l.
FeO	2.65	3.12	1.82	3.40	2.08	2.48
MnO	b.d.l.	b.d.l.	b.d.l.	b.d.l.	b.d.l.	b.d.l.
MgO	2.75	2.51	3.10	2.52	2.85	2.46
CaO	0.02	0.00	0.01	0.16	0.02	0.11
Na_2O	0.52	0.59	0.43	0.74	0.45	0.39
K_2O	10.37	10.91	10.43	9.81	10.19	10.88
Total	96.95	97.28	96.94	97.18	96.65	98.08
Crystal-chemical formula						
O, p.f.u.	11	11	11	11	11	11
Si	3.39	3.36	3.17	3.31	3.40	3.35
Al	2.19	2.21	2.45	2.28	2.18	2.25
Cr	b.d.l.	b.d.l.	b.d.l.	b.d.l.	b.d.l.	b.d.l.
Ti	0.02	0.03	0.05	0.02	0.04	0.03
Fe^{2+}	0.14	0.17	0.10	0.19	0.11	0.13
Mn	b.d.l.	b.d.l.	b.d.l.	b.d.l.	b.d.l.	b.d.l.
Mg	0.27	0.25	0.30	0.25	0.28	0.24
Ca	0.00	0.00	0.00	0.01	0.00	0.01
Na	0.07	0.08	0.05	0.09	0.06	0.05
K	0.87	0.92	0.87	0.82	0.85	0.90
X_{Mg}	0.65	0.59	0.75	0.57	0.71	0.64
Na/(Na + K)	0.07	0.08	0.06	0.10	0.06	0.05

Note. $X_{Mg} = Mg/(Mg + Fe^{2+})$.

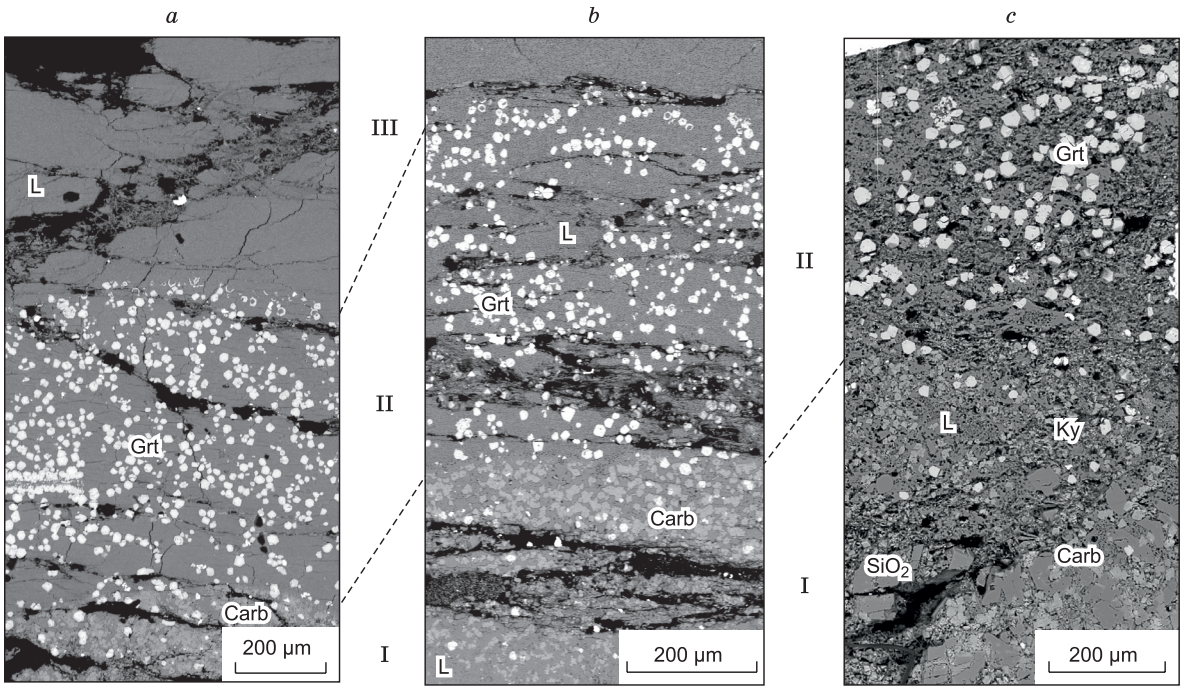

Fig. 5. Correlation of horizontal zoning in welded capsules after runs at 2.9 GPa and different temperatures: *a*, 900 °C (run ss3); *b*, 850 °C (ss2); *c*, 800 °C (ss7). Back-scattered electron images.

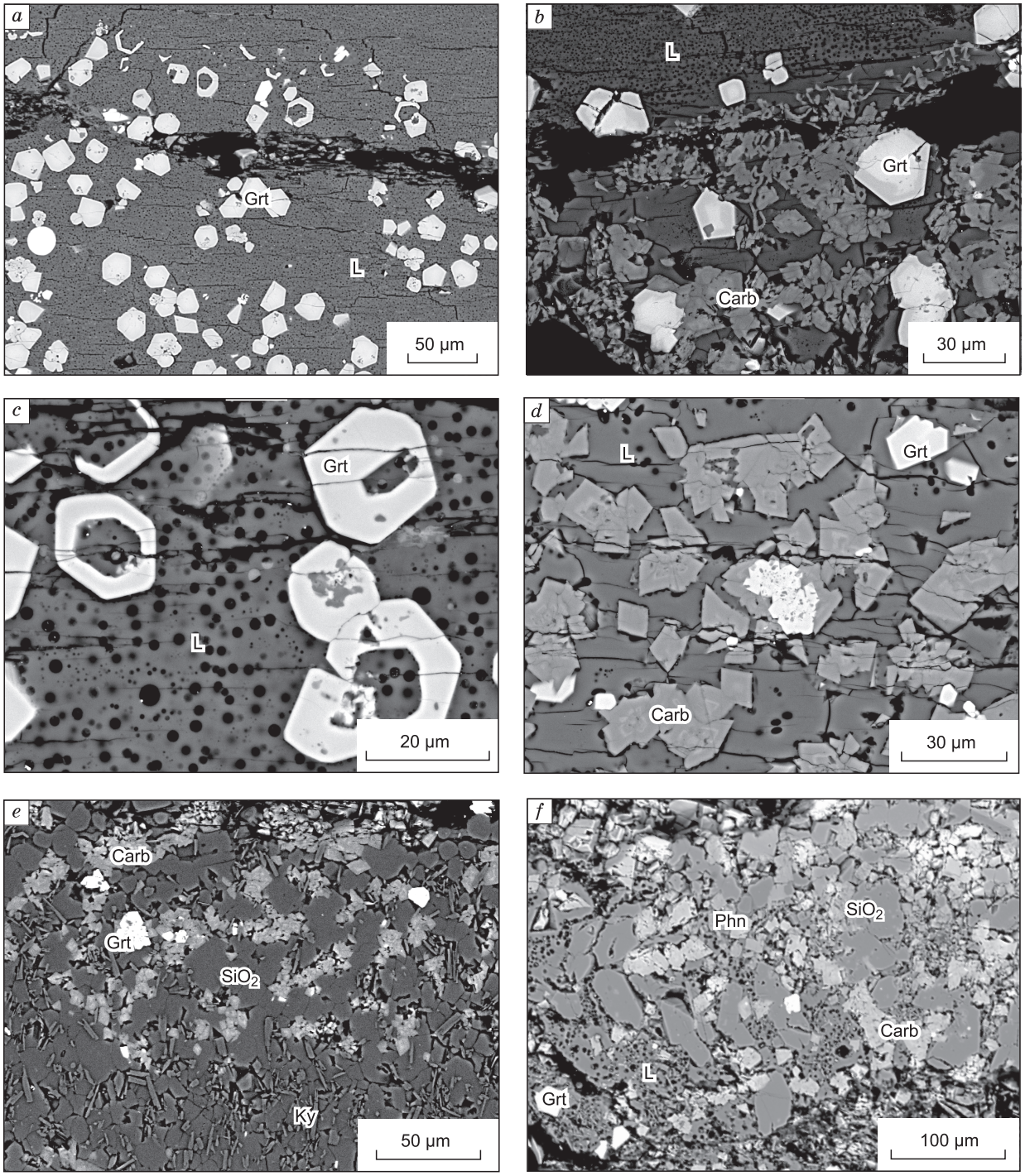

Fig. 6. Phase relations in the run products from welded capsules at 2.9 GPa and different temperatures. *a*, Fragment of zone II with idiomorphic and atoll garnet crystals in glass at the boundary with zone III at 900 °C (run ss3); *b*, fragment with garnet, carbonate, and low-porosity glass from zone I at the boundary with glass from zone II at 900 °C (ss3); *c*, atoll and poikilitic garnets in porous glass from zone II at 850 °C (ss2); *d*, zoned crystals of idiomorphic carbonate and poikilitic garnet in low-porosity glass from zone I at 850 °C (ss2); *e*, phase association without melt at the base of zone I at 850 °C (ss2); *f*, phase association with melt at the base of zone I at 800 °C (ss7).

ence of fluid (mainly H_2O and probably CO_2) in the glasses, and abundant bubbles (Figs. 4, 6) testify to its partial degassing. In melts from open capsules, the lowest silica content is detected in the run at 900 °C; in the runs at 800 and 850 °C, SiO_2 contents overlap (Fig. 9). The content of SiO_2 shows a weak negative correlation with that of Na_2O and total basic oxides (Fig. 9*a*, *b*). Within this temperature interval, the compositions of glasses in welded capsules change

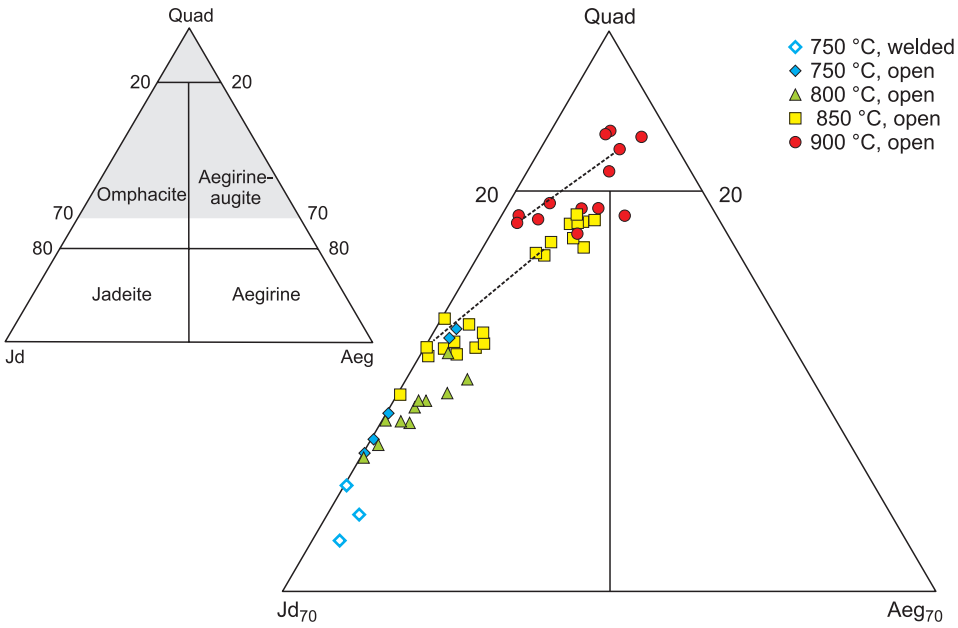

Fig. 7. Compositions of clinopyroxenes from the products of both sets of runs on the Jd–Quad–Aeg classification diagram (Morimoto et al., 1988). Dotted lines connect compositions from zoned grains.

in a similar way (Fig. 9*d*, *e*). In the same runs with welded capsules, there is a weak positive correlation between SiO_2 content and the K_2O/Na_2O ratio (Fig. 9*f*), which is not the case with the runs in open capsules. Comparison of the diagrams shows that the glasses are more sodic in the runs in open capsules than in those in welded capsules. In general, the experimental glasses are characterized by SiO_2 contents high for subduction magmas and the K_2O/Na_2O ratios and total alkalies typical of some adakitic melts (Fig. 9*b*, *c*, *e*, *f*).

Carbonates in most of the runs are present as high-Fe dolomite, in which X_{Ca} varies slightly (0.50–0.58), whereas X_{Mg} = 0.56–0.84 in open capsules and 0.53–0.75 for welded ones (Table 6). As temperature decreases, X_{Mg} decreases. High-Fe magnesite (X_{Mg} = 0.69–0.77, and X_{Ca} = 0.05–0.11) forms instead of dolomite only in an open capsule from the run at 800 °C.

Mica is detected in both sets of runs as phengite (Si = 3.17–3.40 p.f.u., with X_{Mg} = 0.60–0.75 in open capsules and

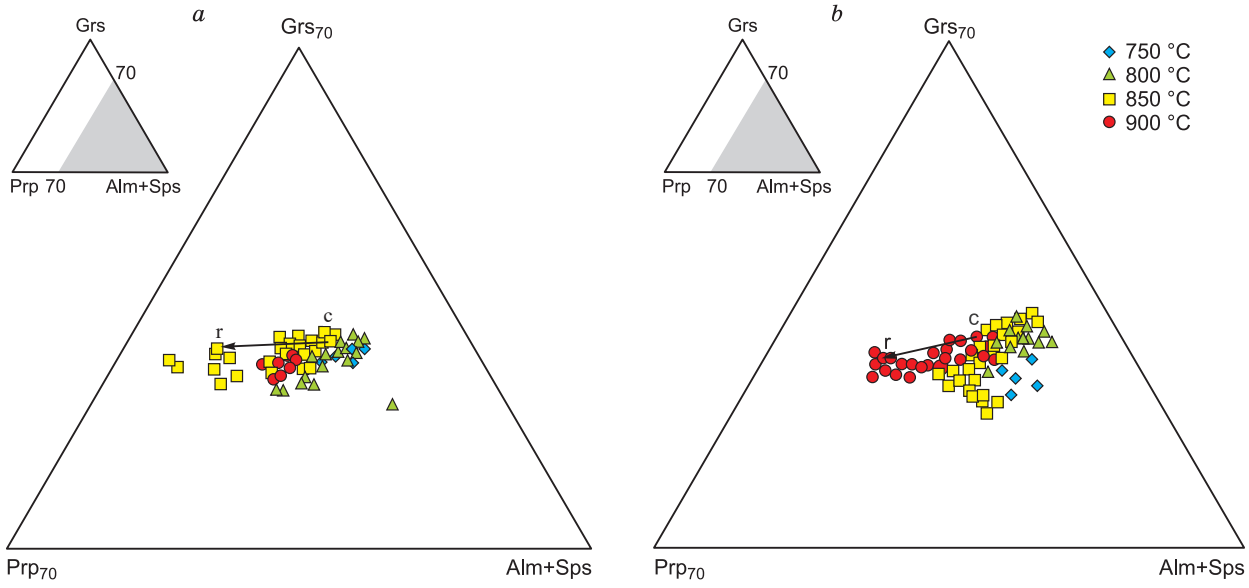

Fig. 8. Compositions of garnets from the run products on the Prp–Grs–(Alm + Sps) diagram: *a*, Open capsules; *b*, welded capsules. Arrows show compositional changes from core to rim in one grain.

0.57–0.71 in welded ones). With increasing temperature, the X_{Mg} value of phengite increases (Table 7).

MODELING OF PHASE EQUILIBRIA

Modeling of phase equilibria is widely used to predict parageneses as well as the contents of volatiles in rocks and their flux from slabs under the *P–T* conditions of subducting plates (Kerrick and Connolly, 2001a; van Keken et al., 2011). Our experimental data on parageneses and the melting of subducting sediment can be compared with the results of thermodynamic modeling presented below.

Modeling of phase equilibria was carried out using the PerpleX software, version 6.8.3 (Connolly, 2005), and a united thermodynamic data set (file hp02ver.dat) (Holland

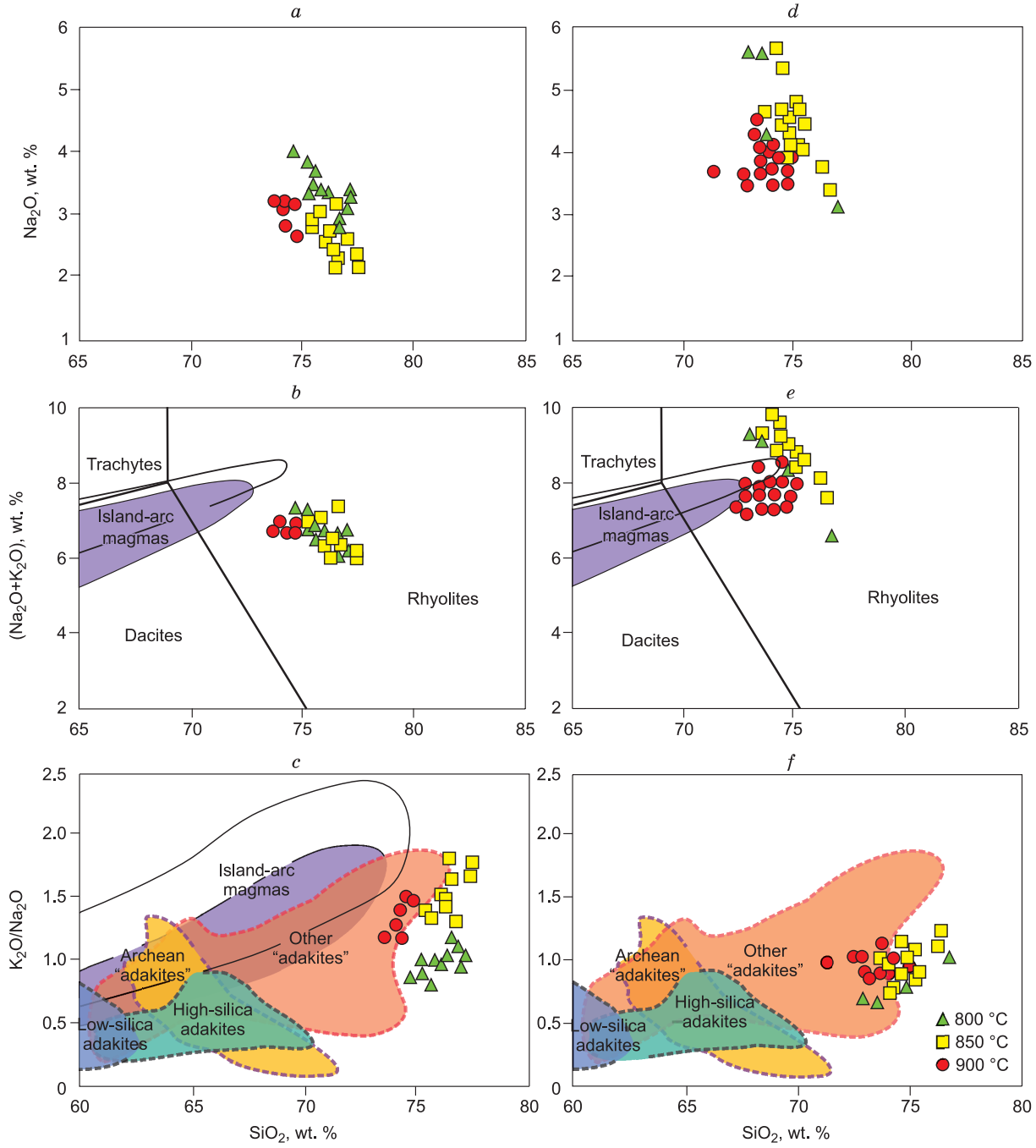

Fig. 9. Normalized compositions of glasses from different sets of runs on diagrams: *a–c*, Open capsules; *d–f*, welded capsules. Compositional fields of adakites and other island-arc magmas (Moyen, 2009) are shown. Fields of island-arc magmas, after (Moyen, 2009): White areas with a black contour indicate "common" island-arc magmas, and lilac areas indicate the products of andesite fractionation. The boundaries of adakite fields, after (Moyen and Martin, 2012; Perchuk et al., 2018a), are marked by dashed lines. See details in the text.

Table 8. Phase composition of subducting sediment (H_2O–GLOSS) under the *P–T* conditions of runs, according to experimental and thermodynamic data obtained using the PerpleX software, version 6.8.3 (Connolly, 2005)

T, °C at 2.9 GPa	Experimental results*		Modeling results**
	Open capsules	Welded capsules	H_2O–GLOSS
750	Grt, Dol, Omp, Ky, SiO_2, Phn	Grt, Dol, Omp, Ky, SiO_2, Phn	Grt(6), Dol(4), Omp(21), Coe(23), Phn(13), H_2O–CO_2 fluid (33)
800	Grt, Mgs, Omp, Ky, SiO_2, Phn, L	Grt, Dol, Ky, SiO_2, Phn, L	Grt(6), Dol(2), Omp(23), Coe(22), Phn(13), H_2O–CO_2 fluid (35)
850	Grt, Dol, Omp, Ky, SiO_2, Phn, L	Grt, Dol, Ky, SiO_2, Phn, L	Grt(8), Omp(22), Q(19), Phn(5), L(13), H_2O–CO_2 fluid (32)
900	Grt, Dol, Omp, L	Grt, Dol, Ky, SiO_2, L	Grt(9), Omp(18), Q(14), L(33), H_2O–CO_2 fluid (26)

*All the phases observed in the products of the experiment are shown.
**For model phases, modes are given in parentheses.

and Powell, 1998; Kerrick and Connolly, 2001a; Ghiorso et al., 2002).

Modeling with regard to melting was done for the composition of subducting sediment used in the runs (H_2O–GLOSS (Table 1)). Besides that, modeling with and with no regard to melting was carried out for GLOSS (Table 1).

Some simplifications were made, which, as we assume, did not have any substantial influence on the result. For example, all Fe was presumed to be in ferrous oxide, whereas titanium, chromium, and manganese oxides were not taken into account because of low contents and/or lacking reliable thermodynamic data for corresponding solid solutions in minerals. Activities for the following minerals were used in the modeling: garnet ((White et al., 2014); Gt(W)), omphacite ((Holland and Powell, 1996); Omph(HP)), carbonates ((Anovitz and Essene, 1987); Cc(EA) and Do(AE)), phengite ((White et al., 2014); Mica(W)), and feldspar ((Fuhrman and Lindsley, 1988), feldspar). The model from ((White et al., 2014), melt(W)), which takes into account H_2O dissolution, was used for melt. For fluid components (H_2O and CO_2), we used the compensated Redlich–Kwong (CORK) equation (Holland and Powell, 1998) and the mixing model from ((Connolly and Trommsdorff, 1991) (F)).

Phase diagram for H_2O–GLOSS. The results of modeling for the composition of the experimental mixture are presented on a phase diagram with a wide temperature and pressure range (Fig. 10*a*); inset shows a detailed diagram for the experimental interval of *P–T* conditions. For the same diagram, we calculated the isolines of H_2O contents in minerals and melt and the isolines of CO_2 contents in minerals (Fig. 10*b*). The distribution of isolines on the *P–T* diagram clearly shows that the content of water in the phases increases dramatically with the start of melting (Fig. 10*b*) because of its dissolution in melt rather than incorporation into the structure of minerals (for example, phengite). On the contrary, the CO_2 content of the phases with increasing temperature decreases to zero under subarc *P–T* conditions in the slabs of hot subduction zones (Fig. 10*b*). Note that the used melt model does not take into account the solubility of CO_2 in felsic magmas at high pressures (Duncan and Dasgupta, 2015), so that the CO_2 isolines might be different under supersolidus conditions.

The modeling permits estimating phase composition and the volume contents of equilibrium phases at each point of the model field, including the *P–T* conditions of the runs (Table 8). We emphasize that the above modal contents of minerals and melt in the capsule (rock) increase considerably after the degassing of the fluid phase. For example, omphacite content in the model paragenesis at 750 °C will be not 21, but rather ~30 vol.%, when corrected for aqueous fluid, which makes up 33 vol.%. The modeling revealed some regularities, which are mainly connected with phase relations during melting. For instance, it was established that melting which starts in the model system at ~820 °C (*P* = 2.9 GPa (Fig. 10*a*)) leads to the disappearance of dolomite at 850 °C and phengite at 870 °C as well as to a decrease in the volume contents (22–38%) of omphacite, SiO_2 phase, and free H_2O–CO_2 fluid. This decrease is observed together with the increasing occurrence of garnet (Table 8).

Phase diagram for GLOSS. Thermodynamic modeling for GLOSS (Plank and Langmuir, 1998) was carried out both with and with no regard to melting. The modeling results for each case are presented on *P–T* diagrams: phase diagram and that with isolines of the contents of volatiles (Fig. 11). The model phase composition and volume contents of phases under the *P–T* conditions of the runs are given in Table 9.

The calculated phase diagrams for GLOSS and H_2O–GLOSS permit discussing the influence of the content of aqueous fluid and melting on parageneses and the fluid content of subducting sediments.

DISCUSSION

Effect of open capsules. The sets of runs with welded and open capsules made it possible to compare the results obtained using different experimental techniques. To begin with, we note similarity of the conditions of the beginning of melting (Fig. 4; Table 8). Pointing out the general similarity between parageneses, we cannot help mentioning differences concerning omphacite. This mineral is widespread in the products of all the runs in open capsules; however, in the runs in welded capsules, it is observed only in the lowest temperature run, which is the only one in the subsolidus

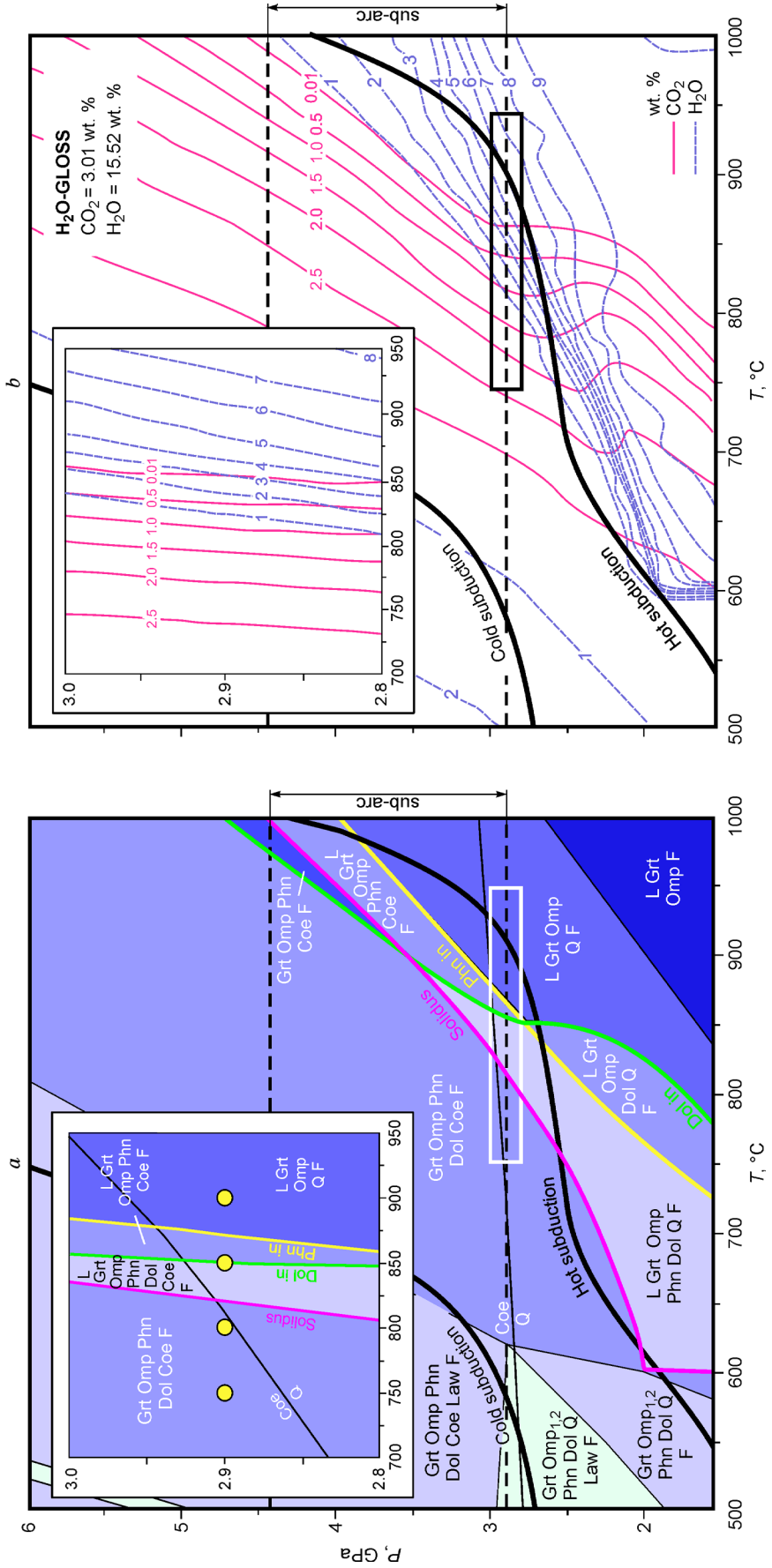

Fig. 10. *P–T* diagrams calculated using the PerpleX software, version 6.8.3 (Connolly, 2005), for H_2O–GLOSS (Table 1). *a*, Phase diagram with melting; *b*, weight contents of H_2O and CO_2 in the phase associations presented in Fig. 10*a*. The weight contents of H_2O and CO_2 in fluid can be obtained by subtraction of the values given on the diagram from the original contents in the initial mixture H_2O–GLOSS. The *P–T* conditions of the runs are shown by dots on insets. Solid lines indicate the hydrous solidus and the boundaries of mineral stability fields. See details in the text.

Table 9. Phase composition and phase contents for GLOSS (Plank and Langmuir, 1998) at 2.9 GPa, from modeling using the PerpleX software, version 6.8.3 (Connolly, 2005), with and without melting

T, °C	GLOSS with melting	GLOSS without melting
750	Grt(6), Dol(6), Omp(25), Coe(29), Phn(17), H_2O–CO_2 fluid (16)	Grt(6), Dol(5), Omp(25), Coe(29), Phn(17), H_2O–CO_2 fluid (16)
800	Grt(6), Dol(5), Omp(27), Coe(29), Phn(17), H_2O–CO_2 fluid (17)	Grt(6), Dol(5), Omp(27), Coe(29), Phn(17), H_2O–CO_2 fluid (17)
850	Grt(7), Dol(4), Omp(25), Q(27), Phn(10), L(12), H_2O–CO_2 fluid (14)	Grt(5), Dol(3), Omp(28), Q(30), Phn(17), H_2O–CO_2 fluid (18)
900	Grt(10), Dol(3), Omp(22), Q(22), Phn(<1), L(32), H_2O–CO_2 fluid (11)	Grt(5), Dol(<1), Omp(30), Q(28), Phn(17), H_2O–CO_2 fluid (20)

Note. Modes of phases are shown in parentheses.

field in this set. We presume that the high partial pressure of H_2O prevented omphacite formation in the presence of melt in welded capsules, whereas the much lower partial pressure in open capsules favored extensive growth of this mineral, including growth from melt.

Comparison between experimental and thermodynamic data. Model parageneses are appropriate for simulating the presence of garnet, omphacite, and SiO_2 phase (up to 850 °C) in open capsules (Fig. 10; Table 8). Melting in the products of this set of runs is observed starting from 800 °C, which is consistent with the calculated line of the hydrous solidus at 820 °C and 2.9 GPa (Fig. 10). Phengite is detected in the runs at ≤850 °C, which agrees well with the calculated field of this mineral, extending up to 870 °C at 2.9 GPa. Note that in the runs with a slightly different composition of sedimentary rock (Table 1) (Hermann and Spandler, 2008), phengite is stable up to a higher temperature (~920 °C) at 2.9 GPa. Carbonates as dolomite (at 800 °C, magnesite) are present among the products of all the runs of this set. According to calculations, dolomite is predicted only in the runs at ≤800 °C. At the same time, the used melt model does not take into account the solubility of CO_2 in felsic magmas at high pressures (Duncan and Dasgupta, 2015); that is, a part of CO_2 might be present not in fluid (as the calculations suggest), but rather in melt. In this case it is likely that dolomite crystals are present in the products of the runs. Kyanite is one more mineral which we see in the runs but not in the calculations. However, kyanite is detected in the products of the runs (at 750–850 °C) in near-accessory contents, so that its absence in the thermodynamic calculations is quite possible.

The above similarities and differences between experimental data for open capsules and model calculations hold true for welded capsules in many respects. In this set of runs, a problem with omphacite arises: This mineral is observed in all the fields of the phase diagram (Fig. 10; Table 8, inset) but not in the products of the supersolidus runs of this set (Fig. 3; Table 2). When interpreting this inconsistency, note that omphacite volume in the model parageneses decreases in the supersolidus field. For example, the appearance of 33 vol.% melt at 900 °C and 2.9 GPa reduces omphacite volume by 20% (Table 8). Therefore, the absence of omphacite in the first approximation in the runs with melting can be regarded as a part of a trend toward a decrease in omphacite content as melt appears, which was detected by thermodynamic modeling (Table 8). On the contrary, in the runs in open capsules under supersolidus conditions, omphacite content increases from 19 to 28 vol.%, respectively (calculations were made using the Corel Photo-Paint 2018 software, based on the number of pixels on BSE images (Fig. 2*a*, *b*)) as temperature increases from 850 to 900 °C.

So, thermodynamic modeling permits a general simulation of parageneses in both open and welded capsules. Note that the trend toward a decrease in omphacite volume with increasing temperature determined during the modeling is consistent with the absence of this mineral in supersolidus runs with welded capsules but inconsistent with its increasing content in open capsules. In this case the modeling was carried out for a thermodynamically isolated system corresponding to runs in welded capsules. Therefore, the question arises if an isolated system corresponds to natural conditions in subduction zones, in which many processes are controlled to a considerable extent by migrating fluids and melts (Spandler and Pirard, 2013; Schmidt and Poli, 2014).

Comparison of results of modeling the compositions of H_2O–GLOSS and GLOSS. The composition of GLOSS differs from that of the mixture used in our runs only in lower water content (Table 1). This permits tracing the influence of the water content of sediment on parageneses and melting processes.

Comparison of phase diagrams for two compositions of subducting sediment (Figs. 10*a*, 11*a*) shows that, as the water content of the model system decreases, the general configuration of the phase diagram is preserved, and so does the position of the hydrous solidus. However, some changes take place; for example, the expansion of the stability fields of phengite and dolomite for GLOSS. Changes in the boundaries of parageneses take place mainly in the high-temperature field, concerning the position of the lines of CO_2 content (Figs. 10*b*, 11*b*): For GLOSS the temperature range of decrease in CO_2 content includes higher temperatures than that for H_2O–GLOSS. Changes in water contents take place within similar ranges of compositions and *P*–*T* conditions. A slight difference is observed for the isolines H_2O = 6 and 7 wt.% in GLOSS, which turn to a low-pressure area at high temperatures. Within a narrower range of *P*–*T* parameters corresponding to the experimental conditions, the modeling predicts a slight change in phase relations compared to H_2O–GLOSS (Tables 8, 9) because of the enlargement of phengite and dolomite stability fields. Notably, the volume contents of most of the minerals (Grt, Dol, SiO_2 phase, and

Phn) and melt for both compositions differ by no more than several vol.% (corrected for fluid volume). At the same time, fluid volume is more than twice higher for H_2O–GLOSS than for GLOSS in the entire experimental range.

The decrease in the water content of subducting sediment from H_2O–GLOSS to GLOSS (Table 1) does not cause any dramatic changes in model parageneses, the *P–T* conditions of the solidus, and the degree of melting in the whole model field. However, significant changes take place in the depth of release of CO_2 from the slab. Modeling for H_2O–GLOSS shows that dolomite is preserved in the slab during cold subduction but completely decomposes in the hot subduction zone at ~2.7 GPa (Fig. 10*b*). For GLOSS, dolomite remains in the slab in different subduction zones, but its quantity is smaller in the case of hot subduction (Fig. 11*b*, *d*). A similar conclusion was made in (Kerrick and Connolly, 2001a): The authors used thermodynamic modeling of GLOSS to demonstrate that decarbonation does not cause release of CO_2 from subducting sediment into the rocks of the mantle wedge. In this case, the liberation of carbonates from the slab might be due to their dissolution by rising flows of water-containing fluid. This mechanism was demonstrated in the runs with carbonate-containing metabasites (Perchuk and Korepanova, 2011; Perchuk et al., 2018a) and in rocks of the Cycladic subduction complex, Greece (Ague and Nicolescu, 2014). The later runs (Perchuk et al., 2019) involving interaction between H_2O–GLOSS and lherzolite showed the small relative volumes of carbonates liberated in this process from the sediment strata at subarc depths of the plate.

Effect of melting on parageneses and fluid content in the GLOSS system. The cited phase relations for GLOSS are based on thermodynamic modeling with no regard to melting (Kerrick and Connolly, 2001a) or on thermodynamic modeling without melting but with correction for this process using experimental data (van Keken et al., 2011). The phase diagrams calculated in the present study for GLOSS with and with no regard to melting permit determining the effect of melting on parageneses and fluid content in sediment. For example, on the phase diagram with melting, phengite disappears at lower temperatures, whereas dolomite disappears at higher temperatures (Fig. 11*a*); on the diagram without melting, the relations are the opposite (Fig. 11*c*). As melting starts, a temperature increase is accompanied by a decrease in the volume contents of omphacite, phengite, and free fluid, whereas garnet content increases (Table 9). If modeling is carried out with no regard to melting, the contents of phases change in the opposite way (Table 9). In this case the content of bound H_2O decreases with increasing temperature (Fig. 11*d*), which differs dramatically from this content in the model with melting (Fig. 11*b*). However, the content of bound CO_2 is only slightly influenced by melting in the system if the melt model does not take into account the dissolution of this component.

Thus, according to thermodynamic modeling, melting has a substantial influence on the modal contents of many minerals and ensures the retention of H_2O in melt.

Application of the experimental results to subduction zones. Magma generation in subduction zones is, to a considerable extent, controlled by partial melting of the suprasubduction mantle in the presence of aqueous fluid (Dobretsov, 2010). Note that magmas generated by partial melting of the rocks of the subducting slab (metasediments and metabasalts) make up a small portion, because this melting requires dramatic heating of the slab surface, which is possible only in "hot" subduction zones. During the formation of such melts, a serious obstacle to their ascent and outflow to the surface is their high viscosity (high silica content), which limits the mobility of melts in the mantle wedge and facilitates their interaction with host peridotites. The last feature is the most important for our runs which show the composition of melts taking active part in both the metasomatism of the mantle wedge and the formation of hybrid melts therein (Spandler and Pirard, 2013; Pirard and Hermann, 2015).

As yet, there are no separate statistical data on felsic magmas molten out of different garnet-containing slab protoliths: metabasites and metasediments. Therefore, we think that natural analogs of experimentally obtained magmas might be some adakites with the highest silica content (Fig. 9, "other adakites") along with adakites with a lower silica content which differently assimilated peridotites of the mantle wedge.

The garnet and clinopyroxene (omphacite) phenocrysts detected in runs with open capsules are not typical of island-arc magmas. Nevertheless, felsic magmas with garnet phenocrysts are recorded, e.g., in the Setouchi volcanic belt, southwestern Japan (Kawabata and Takafuji, 2005). The find of numerous garnet and omphacite phenocrysts in Jurassic felsic lavas in North Ossetia, Caucasus, Russia (Tsvetkov and Borisovskiy, 1980) remains unique. The authors presume that the phenocrysts are xenocrysts—crystals of eclogite minerals trapped by magma, but they do not reject the hypothesis of the magmatic genesis of phenocrysts of high-pressure minerals, the validity of which is confirmed by our runs and the compositions of minerals.

Phengite is the only hydrous mineral in our runs. However, it is not observed in the felsic volcanics of subduction zones, in which other hydrous minerals, such as biotite and amphibole, predominate. This is because biotite and amphibole begin to crystallize in felsic melts formed by metasediments at pressures lower than ~2.5 GPa, whereas magmatic phengite appears at higher pressures (Hermann and Spandler, 2008). The absence of phengite phenocrysts in felsic island-arc magmas suggests that: (1) the magma generation took place at a pressure lower than 2.5 GPa; (2) phengite phenocrysts dissolved in ascending magma as it left the field of thermodynamic stability; (3) phengite dissolved in ascending magma because of a change in its composition during interaction with peridotites or other melts. The last two points might explain why island-arc lavas do not contain carbonate phenocrysts, which are abundant in the run products.

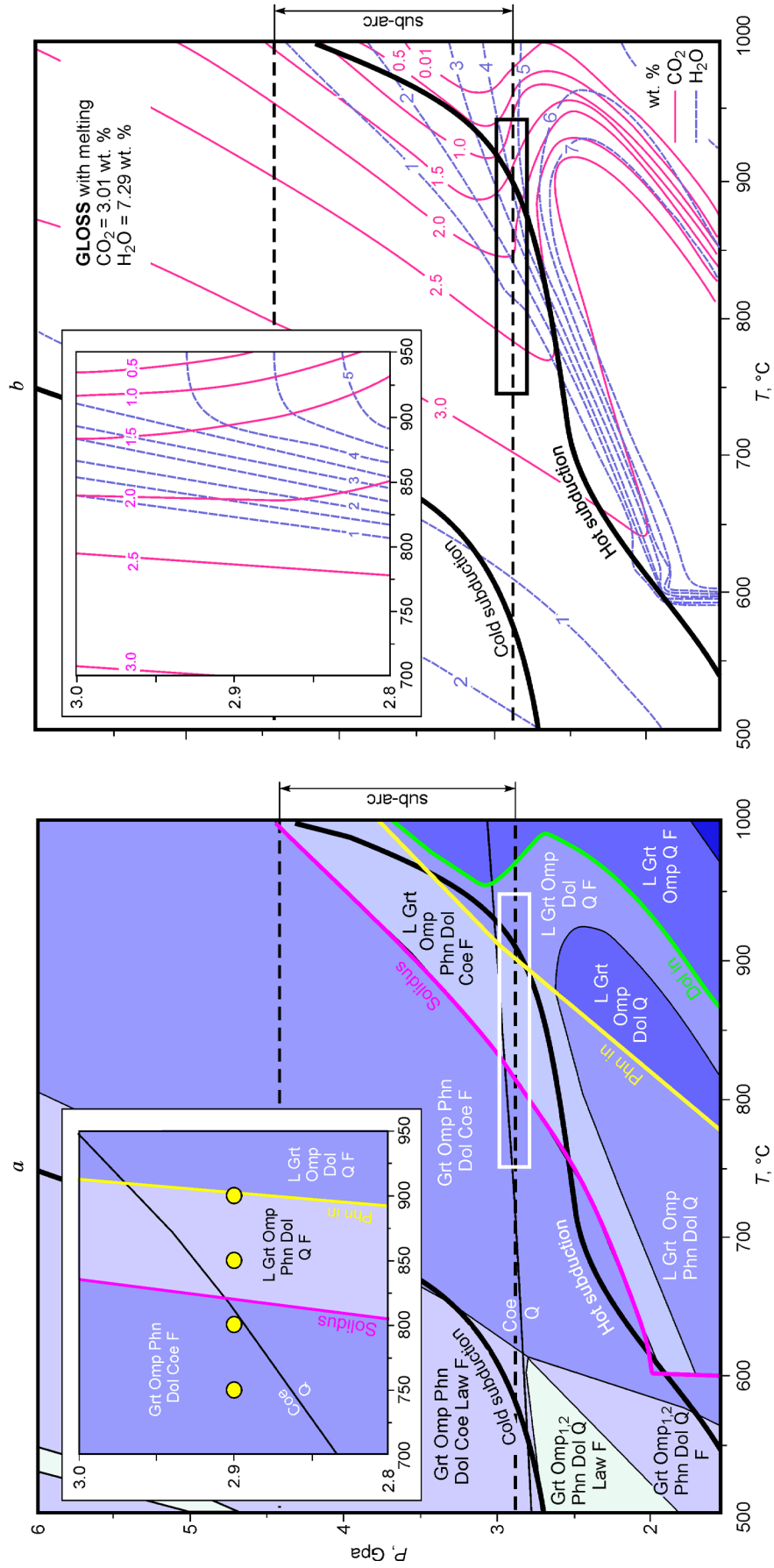

Fig. 11. (*to be continued*).

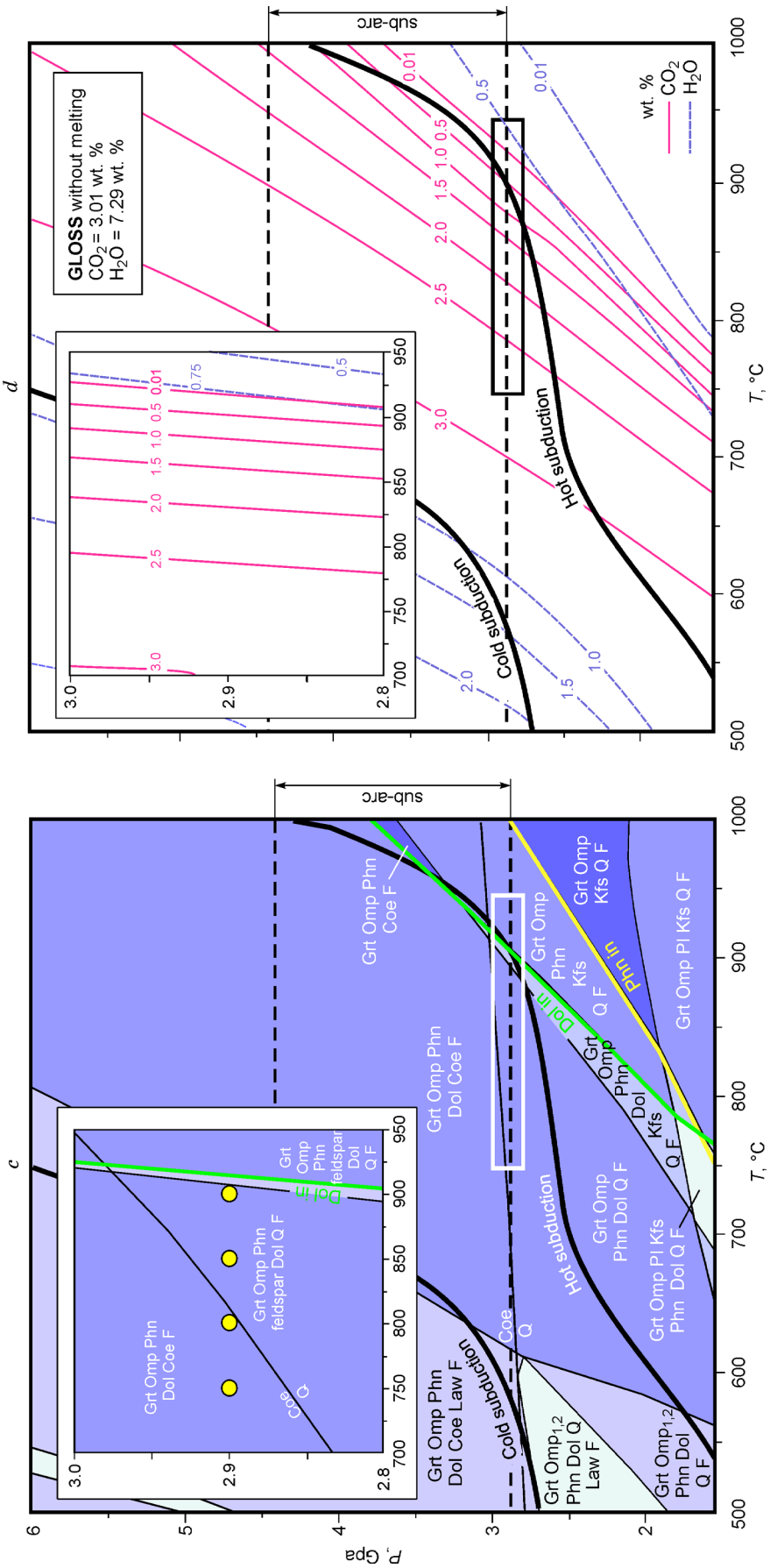

Fig. 11. *P–T* diagrams calculated using the PerpleX software, version 6.8.3 (Connolly, 2005), for GLOSS (Table 1). *a*, Phase diagram with melting; *b*, H_2O and CO_2 contents in the phase associations presented in Fig. 11*a*; *c*, phase diagram without melting; *d*, weight contents of H_2O and CO_2 in the phase associations presented in Fig. 11, *c*. The weight contents of H_2O and CO_2 in fluid can be obtained by subtraction of the values given on the diagram from the original contents in GLOSS (Table 1). Solid lines indicate the hydrous solidus and the boundaries of mineral stability fields. The *P–T* conditions of the runs are shown by dots on insets. See details in the text.

CONCLUSIONS

The experimental study has demonstrated that parageneses of subducting sediment in open and closed systems (capsules) differ in terms of liquids (fluid and melt). Most probably, the high partial pressure of aqueous fluid in welded capsules prevents the formation of omphacite and the eclogite paragenesis. On the contrary, in open capsules, omphacite is a widespread mineral of the eclogite paragenesis, in which it coexists with garnet, kyanite, phengite, and SiO_2 phase. The presence or absence of omphacite in different sets of runs affects the composition of melts, which is less sodic in open capsules than in welded ones. When we choose from the results of the run sets, the tectonic setting of the considered processes is important. The massive fluid flows from different layers of subducting slabs (including those below the sediment strata) predicted on the basis of thermal and petrologic structures in subduction zones (Gorman et al., 2006; Schmidt and Poli, 1998; van Keken et al., 2011) suggest that the results of runs with open capsules are more relevant to this tectonic setting. As thermodynamic modeling of phase equilibria correlates with processes in welded capsules, some corrections to its application for open systems would be beneficial.

The authors thank V.O. Yapaskurt for participation in the microprobe studies; J.A.D. Connolly, for consultations on thermodynamic modeling; S.T. Podgornova, for help with the manuscript preparation; and N.L. Dobretsov and L.Ya. Aranovich, for useful comments, which helped to improve the paper. The studies were made using equipment provided under Moscow University Development Program.

The study was supported by the Russian Foundation for Basic Research (grant no. 16-05-00495).

REFERENCES

Ague, J.J., Nicolescu, S., 2014. Carbon dioxide released from subduction zones by fluid-mediated reactions. Nat. Geosci. 7 (5), 355–360.

Anovitz, L.M., Essene, E.J., 1987. Phase equilibria in the system $CaCO_3$–$MgCO_3$–$FeCO_3$. J. Petrol. 28 (2), 389–415.

Bebout, G.E., 2007. Metamorphic chemical geodynamics of subduction zones. Earth Planet. Sci. Lett. 260 (3), 373–393.

Bose, K., Ganguly, J., 1995. Quartz-coesite transition revisited: Reversed experimental determination at 500–1200 °C and retrieved thermochemical properties. Am. Mineral. 80 (3–4), 231–238.

Brey, G.P., Girnis, A.V., Bulatov, V.K., Höfer, H.E., Gerdes, A., Woodland, A.B., 2015. Reduced sediment melting at 7.5–12 GPa: phase relations, geochemical signals and diamond nucleation. Contrib. Mineral. Petrol. 170, Article 18.

Bulatov, V.K., Brey, G.P., Girnis, A.V., Gerdes, A., Höfer, H.E., 2014. Carbonated sediment–peridotite interaction and melting at 7.5–12 GPa. Lithos 200–201, 368–385.

Connolly, J.A.D., 2005. Computation of phase equilibria by linear programming: A tool for geodynamic modeling and its application to subduction zone decarbonation. Earth Planet. Sci. Lett. 236 (1–2), 524–541.

Connolly, J.A.D., Trommsdorff, V., 1991. Petrogenetic grids for metacarbonate rocks: pressure-temperature phase-diagram projection for mixed-volatile systems. Contrib. Mineral. Petrol. 108 (1), 93–105.

Dobretsov, N.L., 2010. Distinctive petrological, geochemical, and geodynamic features of subduction-related magmatism. Petrology 18 (1), 84–106.

Duncan, M.S., Dasgupta, R., 2015. Pressure and temperature dependence of CO_2 solubility in hydrous rhyolitic melt: implications for carbon transfer to mantle source of volcanic arcs via partial melt of subducting crustal lithologies. Contrib. Mineral. Petrol. 169, Article 54.

Foley, S.F., 2011. A reappraisal of redox melting in the Earth's mantle as a function of tectonic setting and time. J. Petrol. 52 (7–8), 1363–1391.

Fuhrman, M.L., Lindsley, D.H., 1988. Ternary-feldspar modeling and thermometry. Am. Mineral. 73 (3–4), 201–215.

Ghiorso, M.S., Hirschmann, M.M., Reiners, P.W., Kress III, V.C., 2002. The pMELTS: A revision of MELTS for improved calculation of phase relations and major element partitioning related to partial melting of the mantle to 3 GPa. Geochem. Geophys. Geosyst. 3 (5), 1–35.

Gonzalez, C.M., Gorczyk, W., Gerya, T.V., 2016. Decarbonation of subducting slabs: Insight from petrological–thermomechanical modeling. Gondwana Res. 36, 314–332.

Gorman, P.J., Kerrick, D.M., Connolly, J.A.D., 2006. Modeling open system metamorphic decarbonation of subducting slabs. Geochem. Geophys. Geosyst. 7 (4), Q04007.

Grassi, D., Schmidt, M.W., 2011. The melting of carbonated pelites from 70 to 700 km depth. J. Petrol. 52 (4), 765–789.

Hermann, J., Spandler, C.J., 2008. Sediment melts at sub-arc depths: an experimental study. J. Petrol. 49 (4), 717–740.

Hermann, J., Spandler, C., Hack, A., Korsakov, A.V., 2006. Aqueous fluids and hydrous melts in high-pressure and ultra-high pressure rocks: Implications for element transfer in subduction zones. Lithos 92 (3–4), 399–417.

Holland, T.J.B., Powell, R., 1996. Thermodynamics of order-disorder in minerals: 1. Symmetric formalism applied to minerals of fixed composition. Am. Mineral. 81, 1413–1424.

Holland, T.J.B., Powell, R., 1998. An internally consistent thermodynamic data set for phases of petrological interest. J. Metamorph. Geol. 16 (3), 309–343.

Kawabata, H., Takafuji, N., 2005. Origin of garnet crystals in calc-alkaline volcanic rocks from the Setouchi volcanic belt, Japan. Mineral. Mag. 69 (6), 951–971.

Kerrick, D.M., Connolly, J.A.D., 2001a. Metamorphic devolatilization of subducted marine sediments and the transport of volatiles into the Earth's mantle. Nature 411, 293–296.

Kerrick, D.M., Connolly, J.A.D., 2001b. Metamorphic devolatilization of subducted oceanic metabasalts: Implications for seismicity, arc magmatism and volatile recycling. Earth Planet. Sci. Lett. 189 (1–2), 19–29.

Morimoto, N., Fabries, J., Ferguson, A.K., Ginzburg, I.V., Ross, M., Seifert, F.A., Zussman, J., Aoki, K., Gottardi, G., 1988. Nomenclature of pyroxenes. Mineral. Mag. 52 (367), 535–550.

Moyen, J.-F., 2009. High Sr/Y and La/Yb ratios: The meaning of the "adakitic signature." Lithos 112 (3–4), 556–574.

Moyen, J.-F., Martin, H., 2012. Forty years of TTG research. Lithos 148, 312–336.

Patiño Douce, A.E., Harris, N., 1998. Experimental constraints on Himalayan anatexis. J. Petrol. 39 (4), 689–710.

Perchuk, A.L., Korepanova, O.S., 2011. The problem of CO_2 recycling in subduction zones. Moscow Univ. Geol. Bull. 66 (4), 250–260.

Perchuk, A.L., Shur, M.Yu., Yapaskurt, V.O., Podgornova, S.T., 2013. Experimental modeling of mantle metasomatism coupled with eclogitization of crustal material in a subduction zone. Petrology 21 (6), 579–598.

Perchuk, A.L., Yapaskurt, V.O., Griffin, W.L., Shur, M.Yu., Gain, S.E.M., 2018a. Three types of element fluxes from metabasite into peridotite

in analogue experiments: Insights into subduction-zone processes. Lithos 302–303, 203–223.

Perchuk, A.L., Yapaskurt, V.O., Zinovieva, N.G., Shur, M.Yu., 2018b. Experimental evidence for opposite fluxes of sodium, potassium, and CO_2 during glaucophane schist interaction with harzburgite and websterite in subduction zones. Petrology 26 (6), 599–616.

Perchuk, A.L., Serdyuk, A.A., Zinovieva, N.G., 2019. Subduction sediment–lherzolite interaction at 2.9 GPa: effects of metasomatism and partial melting. Petrology 27 (5), 467–488.

Pirard, C., Hermann, J., 2015. Focused fluid transfer through the mantle above subduction zones. Geology 43 (10), 915–918.

Plank, T., Langmuir, C.H., 1998. The geochemical composition of subducting sediment and its consequences for the crust and mantle. Chem. Geol. 145, 325–394.

Scambelluri, M., Philippot, P., 2001. Deep fluids in subduction zones. Lithos 55 (1–4), 213–227.

Schmidt, M.W., Poli, S., 1998. Experimentally based water budgets for dehydrating slabs and consequences for arc magma generation. Earth Planet. Sci. Lett. 163 (1–4), 361–379.

Schmidt, M.W., Poli, S., 2014. Devolatilization during subduction, in: Holland, H.D., Turekian, K.K. (Eds.), Treatise on Geochemistry, 2nd ed. Elsevier, Amsterdam. Vol. 4: The Crust, pp. 669–701.

Spandler, C., Pirard, C., 2013. Element recycling from subducting slabs to arc crust: A review. Lithos 170–171, 208–223.

Syracuse, E.M., van Keken, P.E., Abers, G.A., 2010. The global range of subduction zone thermal models. Phys. Earth Planet. Int. 183 (1–2), 73–90.

Tatsumi, Y., Eggins, S.M., 1995. Subduction Zone Magmatism. Blackwell, Oxford.

Tsvetkov, A.A., Borisovskiy, S.Y., 1980. High-pressure minerals in Jurassic andesite-dacite lavas from Northern Osetia. Int. Geol. Rev. 22 (3), 297–306.

van Keken, P.E., Hacker, B.R., Syracuse, E.M., Abers, G.A., 2011. Subduction factory: 4. Depth-dependent flux of H_2O from subducting slabs worldwide. J. Geophys. Res. 116, B01401.

White, R.W., Powell, R., Johnson, T.E., 2014. The effect of Mn on mineral stability in metapelites revisited: New *a–x* relations for manganese-bearing minerals. J. Metamorph. Geol. 32 (8), 809–828.

Woodland, A.B., Bulatov, V.K., Brey, G.P., Girnis, A.V., Höfer, H.E. Gerdes, A., 2018. Subduction factory in an ampoule: Experiments on sediment–peridotite interaction under temperature gradient conditions. Geochim. Cosmochim. Acta 223, 319–349.

Zheng, Y.-F., 2019. Subduction zone geochemistry. Geosci. Front., doi.org/10.1016/j.gsf.2019.02.003.

Editorial responsibility: N.V. Sobolev